KMT-2016-BLG-2052L: Microlensing Binary Composed of M Dwarfs Revealed from a Very Long Timescale Event

Cheongho Han[1] , Youn Kil Jung[2,15], Yossi Shvartzvald[3,15,16],
and
Michael D. Albrow[4], Sun-Ju Chung[2,5], Andrew Gould[2,6,7], Kyu-Ha Hwang[2], Doeon Kim[1], Chung-Uk Lee[2], Woong-Tae Kim[8] ,
Hyoun-Woo Kim[2], Yoon-Hyun Ryu[2] , In-Gu Shin[9] , Jennifer C. Yee[9], Chun-Hwey Kim[10] , Sang-Mok Cha[2,11],
Seung-Lee Kim[2,5], Dong-Jin Kim[2], Dong-Joo Lee[2], Yongseok Lee[2,11], Byeong-Gon Park[2,5], Richard W. Pogge[6]
(The KMTNet Collaboration),
and
Charles Beichman[12], Geoff Bryden[13], Sebastiano Calchi Novati[3], B. Scott Gaudi[6], Calen B. Henderson[12], T. P. Matthew[6], and
Savannah R. Jacklin[14]
(The UKIRT Microlensing Team)
[1] Department of Physics, Chungbuk National University, Cheongju 28644, Republic of Korea; cheongho@astroph.chungbuk.ac.kr
[2] Korea Astronomy and Space Science Institute, Daejon 34055, Republic of Korea
[3] IPAC, Mail Code 100-22, Caltech, 1200 E. California Blvd., Pasadena, CA 91125, USA
[4] University of Canterbury, Department of Physics and Astronomy, Private Bag 4800, Christchurch 8020, New Zealand
[5] Korea University of Science and Technology, 217 Gajeong-ro, Yuseong-gu, Daejeon 34113, Republic of Korea
[6] Department of Astronomy, Ohio State University, 140 W. 18th Ave., Columbus, OH 43210, USA
[7] Max Planck Institute for Astronomy, Königstuhl 17, D-69117 Heidelberg, Germany
[8] Department of Physics & Astronomy, Seoul National University, Seoul 151-742, Republic of Korea
[9] Harvard-Smithsonian Center for Astrophysics, 60 Garden St., MS-15 Cambridge, MA, 02138, USA
[10] Department of Astronomy and Space Science, Chungbuk National University, Cheongju 28644, Republic of Korea
[11] School of Space Research, Kyung Hee University, Yongin 17104, Republic of Korea
[12] IPAC/NExScI, Mail Code 100-22, Caltech, 1200 E. California Blvd., Pasadena, CA 91125, USA
[13] Jet Propulsion Laboratory, California Institute of Technology, 4800 Oak Grove Dr., Pasadena, CA 91109, USA
[14] Vanderbilt University, Department of Physics & Astronomy, Nashville, TN 37235, USA

Abstract

We present the analysis of a binary microlensing event, KMT-2016-BLG-2052, for which the lensing-induced brightening of the source star lasted for two seasons. We determine the lens mass from the combined measurements of the microlens parallax, π_E, and angular Einstein radius, θ_E. The measured mass indicates that the lens is a binary composed of M dwarfs with masses of $M_1 \sim 0.34\,M_\odot$ and $M_2 \sim 0.17\,M_\odot$. The measured relative lens-source proper motion of $\mu \sim 3.9$ mas yr^{-1} is smaller than ~ 5 mas yr^{-1} of typical Galactic lensing events, while the estimated angular Einstein radius of $\theta_E \sim 1.2$ mas is substantially greater than the typical value of ~ 0.5 mas. Therefore, it turns out that the long timescale of the event is caused by the combination of the slow μ and large θ_E rather than the heavy mass of the lens. From the simulation of Galactic lensing events with very long timescales ($t_E \gtrsim 100$ days), we find that the probabilities that long timescale events are produced by lenses with masses $\geqslant 1.0\,M_\odot$ and $\geqslant 3.0\,M_\odot$ are $\sim 19\%$ and 2.6%, respectively, indicating that events produced by heavy lenses comprise a minor fraction of long timescale events. The results indicate that it is essential to determine lens masses by measuring both π_E and θ_E in order to firmly identify heavy stellar remnants, such as neutron stars and black holes.

Key words: binaries: general – gravitational lensing: micro

1. Introduction

From dozens per year when the first-generation microlensing experiments (Alcock et al. 1993; Aubourg et al. 1993; Udalski et al. 1993) were conducted, the detection rate of microlensing events has greatly increased, and currently more than 2500 microlensing events are annually detected (Bond et al. 2001; Udalski et al. 2015; Kim et al. 2018b). The dramatic increase of the event rate became possible by various factors, including the development of advanced event finding algorithms, the increased observational cadence thanks to upgraded instruments, and the

addition of new surveys. As the event rate increases, the scientific scope of microlensing has also expanded from the original use of detecting Galactic dark matter in the form of massive compact halo objects (Paczyński 1986) into various fields, including extrasolar planet searches (Mao & Paczynski 1991; Gould & Loeb 1992).

A small fraction of microlensing events last for very long durations. Such long timescale events are of scientific importance for various reasons. First, lenses of these events are candidates of heavy stellar remnants such as neutron stars (NSs) and black holes (BHs) (Shvartzvald et al. 2015; Wyrzykowski et al. 2016). The event timescale, which is defined as the time for the source to cross the angular Einstein radius, θ_E, of the lens, is related to the physical parameters of

---

the lens system by

$$t_{\rm E} = \frac{\theta_{\rm E}}{\mu} = \frac{\sqrt{\kappa M \pi_{\rm rel}}}{\mu}, \qquad (1)$$

where M is the lens mass, μ is the relative lens-source proper motion, $\kappa = 4G/(c^2{\rm au})$, $\pi_{\rm rel} = \pi_{\rm L} - \pi_{\rm S} = {\rm au}(D_{\rm L}^{-1} - D_{\rm S}^{-1})$ represents the relative lens-source parallax, and $D_{\rm L}$ and $D_{\rm S}$ denote the distances to the lens and source, respectively. First, because the timescale is proportional to the square root of the lens mass, very long timescale events are more likely to be produced by heavy lenses. Second, the chance to measure a microlens parallax, $\pi_{\rm E}$, is high for long timescale events. As an event timescale approaches or exceeds the orbital period of Earth, i.e., 1 yr, the relative lens-source motion departs from being rectilinear due to Earth's orbital motion. This induces long-term deviations in lensing light curves, microlens-parallax effects, and the analysis of the deviation yields $\pi_{\rm E}$ (Gould 1992). The microlens parallax is related to the lens mass and distance by

$$M = \frac{\theta_{\rm E}}{\kappa \pi_{\rm E}} \qquad (2)$$

and

$$D_{\rm L} = \frac{\rm au}{\pi_{\rm E}\theta_{\rm E} + \pi_{\rm S}}, \qquad (3)$$

respectively (Gould 2000b). Therefore, the physical lens parameters can be significantly better defined with the additional constraint of the microlens parallax (Han & Gould 1995). Third, long timescale events produced by binary lenses are especially important because one can additionally measure the angular Einstein radius. This is because binary-lens events usually produce caustic-crossing features in lensing light curves. This part of the light curve is affected by finite-source effects, and the analysis of the deviation enables one to measure the Einstein radius. With the measurement of both $\pi_{\rm E}$ and $\theta_{\rm E}$, the lens mass can be uniquely determined, and the nature of the lens can be revealed.

In this work, we present the analysis of a binary microlensing event, KMT-2016-BLG-2052. For the event, the lensing-induced magnification of the source flux lasted for two years from the beginning of the 2016 bulge season until the end of the 2017 season. The light curve of the event also exhibits a caustic-crossing feature that was densely resolved. We characterize the lens by estimating the mass from the simultaneous measurements of $\pi_{\rm E}$ and $\theta_{\rm E}$.

2. Observation and Data

The lensing event KMT-2016-BLG-2052 occurred on a star located toward the Galactic bulge field with the equatorial coordinates (R.A., decl.)$_{\rm J2000}$ = (17:41:19.50, −27:40:19.67), which corresponds to Galactic coordinates $(l, b) = (0°.58, 1°.47)$. Due to the closeness to the Galactic center, the source star was heavily extinct by dust.

The event was identified by applying the Event Finder algorithm (Kim et al. 2018a, 2018b) to the 2016 season data acquired by Korea Microlensing Telescope Network (KMTNet) survey (Kim et al. 2016). The survey uses three identical 1.6 m telescopes that are globally located at the Cerro

Tololo Interamerican Observatory in Chile, the South African Astronomical Observatory in South Africa, and the Siding Spring Observatory in Australia. We designates the individual KMTNet telescopes as KMTC, KMTS, and KMTA, respectively. The observations were conducted mostly in I band with occasional V-band observations for the source color measurement. The source is located in the BLG15 field for which observations were conducted at one-hour cadence. The data were reduced using the pySIS photometry software package (Albrow et al. 2009) that was developed on the basis of the Difference Image Analysis technique (Alard & Lupton 1998; Woźniak 2000). For the KMTC data set, additional photometry is conducted using the software package DoPHOT (Schechter et al. 1993) for the construction of color–magnitude diagram and the measurement of the source color. The data sets used in the analysis are composed of 1168, 1132, and 410 points collected from the KMTC, KMTS, and KMTA observations, respectively.

The event was also observed in the 2015 and 2017 seasons using the 3.8 m United Kingdom Infrared Telescope (UKIRT Microlensing survey; Shvartzvald et al. 2017). UKIRT observations were conducted in H band, and aperture photometry is used for reduction. The data were used for the source color measurement. The UKIRT data set is composed of 142 and 75 points taken during the 2015 and 2017 seasons, respectively.

In Figure 1, we present the light curve of the event. The most important characteristics of the event is its long duration. The lensing-induced magnification of the source flux started from the beginning of the 2016 bulge season and continued until the end of the season. Due to the scientific importance of a long timescale caustic-crossing binary-lens event, we have incorporated additional data from the 2017 season. Surprisingly, the event continued until the end of the 2017 season. The light curve is featured by a bump centered at ${\rm HJD}' = {\rm HJD} - 2450000 \sim 7600$ and by a sharp spike at ${\rm HJD}' \sim 7630$. See Figure 2, where we present the enlarged view around the features. These bump and spike features are produced when a source approaches close to the cusp and passes over the fold of a caustic formed by a binary lens, respectively. Binary-lens caustics form closed curves, and thus caustic crossings occur in pairs, and the light curve between the caustic crossings is characterized by a "U"-shape trough. From the partial U-shape feature observed during $7630 \lesssim {\rm HJD}' \lesssim 7680$, it is very likely that the second caustic crossing (and, possibly, additional caustic-related features) occurred during the four month period when the bulge field was not observed as it passed behind the Sun. Because the event did not return to the baseline until the end of the 2017 season, we incorporate additional data collected during the 2018 season in the analysis for the secure baseline measurement.

3. Analysis

Because the bump and spike are characteristic features of binary-lens events, we conduct modeling of the observed light curve based on the binary-lens interpretation. Under the assumption that there is no acceleration in the relative lens-source motion, a binary-lensing light curve is described by seven principal parameters. Four of these parameters describe the lens-source approach including the time of the closest source approach to a reference position of the lens, t_0; the source-reference separation at that time, u_0; the event timescale, $t_{\rm E}$; and the angle
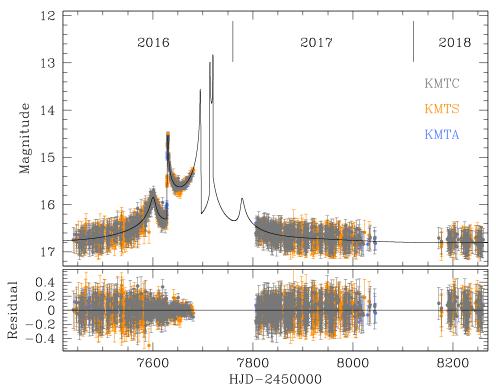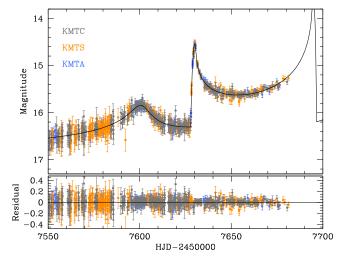
Figure 1. Light curve of KMT-2016-BLG-2052. The curve superposed on the data points represents the binary-lensing model. The bottom panel shows the residual from the model.

Figure 2. Enlarged view of the light curve covering the observed portion of the features induced by the binary caustic.

between the source trajectory and the binary axis, α (the source trajectory angle). For the reference lens position, we use the center of mass. Two parameters, s and q, represent the projected separation (normalized to θ_E) and mass ratio between the binary-lens components, respectively. The last parameter, ρ, which is defined as the ratio of the angular source radius θ_* to θ_E (normalized source radius), is needed to account for finite-source effects that cause deviations in lensing light curves when the source crosses over or approaches close to caustics.

We begin modeling the light curve with the principal binary-lensing parameters under the assumption that the relative lens-source motion is rectilinear. The modeling is conducted in two steps. In the first step, we conduct a grid search for s and q,

while the other parameters are searched for using a downhill approach based on the Markov Chain Monte Carlo (MCMC) method. This preliminary search yields a χ^2 map in the $(\log s, \log q)$ plane from which we identify local minima and possible degenerate solutions. Because the nature of the lens is not known in advance, we inspect a wide range of binary separations and mass ratios. The inspected ranges are $-1.0 < \log s < 1.0$ and $-5.0 < \log q < 1.0$. For the local minima found from this preliminary search, we then refine the solutions by allowing all lensing parameters to vary. From this preliminary modeling, we identify a solution with $s \sim 1.4$ and $q \sim 0.26$. The model describes the overall light curve. However, it leaves substantial residuals, especially around the main features of the bump and the caustic-crossing spike.

Because the event lasted for ~ 2 yr, the assumption of a rectilinear relative lens-source motion may not be valid due to either the orbital motion of the observer, i.e., Earth, or of the binary lens. We, therefore, test whether the fit improves with the consideration of the higher-order effects caused by the orbital motions of Earth (the microlens-parallax effect) and the lens (the lens-orbital effect). Modeling the light curve considering the microlens-parallax effect requires two additional parameters, $\pi_{E,N}$ and $\pi_{E,E}$, which denote the north and east components of the microlens-parallax vector $\boldsymbol{\pi}_E = (\pi_{rel}/\theta_E)(\boldsymbol{\mu}/\mu)$, respectively. Consideration of the lens-orbital motion also requires us to include additional parameters. Under the approximation that the positional changes of the lens components are small during the event, the effect is described by the two parameters of ds/dt and $d\alpha/dt$, which denote the change rates of the binary separation and the orientation angle of the binary axis relative to the source trajectory, respectively. When microlens-parallax effects are considered, a pair of degenerate solutions are
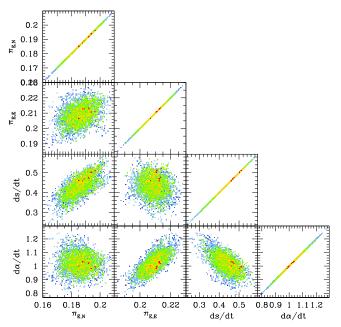
Table 1
Comparison of Models

Model		χ^2
Standard		3159.7
Orbit		2721.8
Parallax	$(u_0 > 0)$	2712.6
	$(u_0 < 0)$	2712.7
Orbit+Parallax	$(u_0 > 0)$	2675.2
	$(u_0 < 0)$	2691.2

known to exist with $u_0 > 0$ and $u_0 < 0$ due to mirror symmetry of the source trajectory with respect to the binary axis: "ecliptic degeneracy" (Smith et al. 2003; Skowron et al. 2011). Therefore, we test the degeneracy whenever microlens-parallax effects are considered.
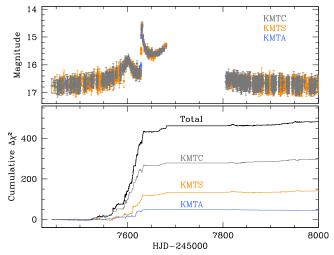
In Table 1, we list the χ^2 values of the tested models. The "standard" model designates the solution obtained under the assumption of a rectilinear relative lens-source motion. In the "orbit" and "parallax" models, we separately consider the lens-orbital and microlens-parallax effects, respectively. In the "orbit+parallax" model, we simultaneously consider both higher-order effects. We find that higher-order effects greatly improve the fits. As measured by the difference in the χ^2 values, the improvement is $\Delta\chi^2 \sim 434$ and ~ 447 with respect to the standard model when the lens-orbital and microlens-parallax effects are separately considered, respectively. When both higher-order effects are simultaneously considered, the fit improves by $\Delta\chi^2 \sim 485$. We found that the degeneracy between $u_0 > 0$ and $u_0 < 0$ solutions is moderately severe with $\Delta\chi^2 \sim 16$. Considering that the improvements by the individual higher-order effects are similar, it is likely that both the microlens-parallax and lens-orbital effects are important to describe precisely the observed light curve. Both higher-order effects are known to cause qualitatively similar deviations in lensing light curves (Batista et al. 2011; Skowron et al. 2011; Han et al. 2016). In Figure 3, we present the $\Delta\chi^2$ distributions of the MCMC points in the planes of the higher-order lensing parameter pairs to show the correlations between the higher-order lensing parameters. It shows that the $\pi_{E,N}$–ds/dt and $\pi_{E,E}$–$d\alpha/dt$ parameter pairs are closely correlated. To check the region of the fit improvement by the higher-order effects, in Figure 4, we plot the cumulative distribution of $\Delta\chi^2$ between the models with and without the higher-order effects. For all data sets, the fit improves throughout the event.

In Table 2, we present the lensing parameters of the best-fit solutions. Because the degeneracy between the $u_0 > 0$ and $u_0 < 0$ solutions is moderately severe, we present the lensing parameters of both solutions. From the lensing parameters, we found that the event was produced by a binary with a mass ratio of $q \sim 0.5$ and a projected separation very close to the Einstein radius, i.e., $s \sim 1.0$. As anticipated, the measured event timescale, $t_E \sim 112$ days, is very long. We note that the lensing parameters of the $u_0 > 0$ and $u_0 < 0$ solutions are roughly in the relation $(u_0, \alpha, \pi_{E,N}, d\alpha/dt) \leftrightarrow -(u_0, \alpha, \pi_{E,N}, d\alpha/dt)$ due to the mirror symmetry of the lens-system configuration (Skowron et al. 2011).

In Figure 5, we present the lens-system configuration in which the source trajectory (curve with an arrow) with respect to the caustic (closed curve with 6 cusps) and the individual lens components (open circles marked by M_1 and M_2) are shown. The presented configuration is for the $u_0 > 0$ solutions. We note that the configuration of the $u_0 < 0$ solution is almost

Figure 3. Distributions of $\Delta\chi^2$ in the planes of the higher-order lensing parameter pairs. The color coding indicates points in the MCMC chain within 1σ (red), 2σ (yellow), 3σ (green), 4σ (cyan), and 5σ (blue) with respect to the best-fit value. The distributions are for the $u_0 > 0$ solution.
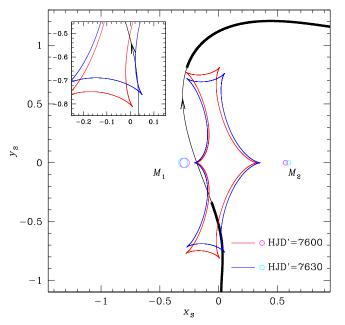

Figure 4. Cumulative distribution of $\Delta\chi^2$ between the models with and without the higher-order effects. The thick black solid curve is for the whole data and the thin curves with different colors are for the individual data sets. The light curve in the upper panel is presented to show the region of fit improvement.

in mirror symmetry with respect to the M_1–M_2 axis compared to the $u_0 > 0$ solution. Because the lens positions and the resulting shape of the caustic vary in time due to the change of the binary separation caused by the lens-orbital effect, we present caustics at two epochs of $HJD' = 7600$ (at the time of the bump) and $HJD' = 7630$ (at the time of the caustic entrance). Due to the closeness of the binary separation to unity, the caustic forms a closed curve with six cusps and folds, i.e., a resonant caustic. The configuration shows that the source approached close to the cusp located in the lower right part of the caustic, producing the bump, and passed over the adjacent fold of the caustic, producing the caustic-crossing spike. The U-shape trough was produced during the passage of the source inside the caustic. According to the best-fit model, the source

Table 2
Best-fit Lensing Parameters

Parameter	$u_0 > 0$	$u_0 < 0$
t_0 (HJD')	7709.427 ± 0.823	7709.939 ± 0.592
u_0	0.174 ± 0.009	-0.204 ± 0.006
t_E (days)	111.53 ± 0.78	112.57 ± 0.45
s	0.957 ± 0.005	0.958 ± 0.001
q	0.507 ± 0.011	0.525 ± 0.011
α (rad)	4.258 ± 0.022	-4.206 ± 0.011
ρ (10^{-3})	2.71 ± 0.07	2.84 ± 0.04
$\pi_{E,N}$	0.193 ± 0.008	0.210 ± 0.009
$\pi_{E,E}$	0.211 ± 0.006	0.192 ± 0.008
ds/dt (yr^{-1})	0.503 ± 0.049	0.467 ± 0.012
$d\alpha/dt$ (rad yr^{-1})	0.984 ± 0.068	-0.956 ± 0.090

Note. HJD' = HJD − 2450000.

Figure 6. Variation of the unobserved part of the light curve. Presented are the model light curves for four different solutions within 3σ level from the best-fit solution (black curve).
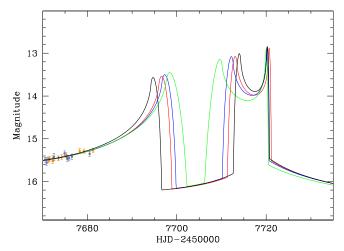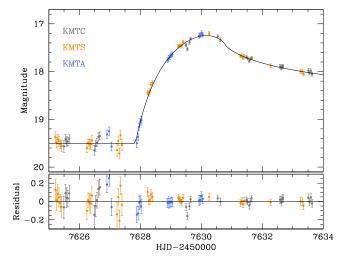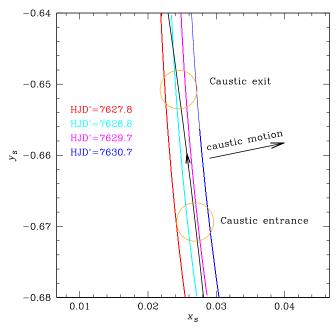

Figure 5. Configurations of the lens system. The curve with an arrow is the source trajectory, and the cuspy closed figure represents the caustics. The small open circles marked by M_1 and M_2 represent the positions of the lens components. Because the lens position and the caustic shape vary due to the orbital motion, we present lens positions and caustics at two epochs of HJD' = 7600 and 7630. The part of the source trajectory marked by a thin line represents the region during which the bulge field was not observed as it passed behind the Sun. The inset shows the zoom around the region of the caustic entrance. Coordinates are centered at the barycenter of the binary lens, and lengths are scaled to the Einstein radius corresponding to the total mass of the lens.

Figure 7. Zoom of the light curve around the time of the caustic crossing. The curve plotted over data points is the model light curve.

exited the caustic by passing over the lower left fold at HJD' ∼ 7695 (2016 November 2). Then, the source additionally passed the tip of the nearby cusp on HJD' ∼ 7715 (2016 November 22) and approached the tip of the upper left cusp on HJD' ∼ 7778 (2017 January 24), resulting in a multiple-peak light curve. Unfortunately, these additional features were not be covered because the bulge could not be observed from Earth.

We note that the lensing parameters could have been better constrained if these additional caustic-related features could have been observed. This is because these features are very sensitive to the small changes in the lensing parameters due to the special lens-system configuration in which the source

approaches very close to the caustic. The high sensitivity of the unseen caustic features to the lensing parameters is demonstrated in Figure 6, where we present model light curves for 4 different solutions within 3σ level from the best-fit solution (black curve). We found that the model light curve significantly varies even for slight differences in the lensing parameters. Multiple-peak features in lensing light curves are known to help better constrain lens systems (An & Gould 2001; Udalski et al. 2018). If they had been observed, then the lensing parameters (especially the higher-order parameters) could have been determined with improved precision and accuracy.

Finite-source effects are clearly detected during the caustic crossing. In Figure 7, we present the zoom of the light curve around the time of the caustic entrance. It shows that the crossing, which lasted for about three days, was densely and continuously covered from the combined observations using the globally distributed telescopes. An analysis of this part of the light curve yields a normalized source radius of $\rho \sim 2.7 \times 10^{-3}$ and a source self-crossing timescale of $t_* = \rho t_E \sim 0.3$ days. The duration between the time of the source star's touch to the fold of the caustic, at $\mathrm{HJD}'_1 = 7627.8$, and the peak of the caustic crossing, at $\mathrm{HJD}'_2 = 7630.2$, is

Figure 8. Zoom of the caustic configuration around the time of the caustic crossing. The four curves in different colors represent fold caustics at different times marked in the legend, and the line with an arrow is the source trajectory. The two orange circles represent the source at the beginning and the end of the caustic crossing.

$\Delta t \sim 2.4$ days. For a static caustic, this duration corresponds to $\Delta t = 1.7(t_*/\sin\phi)$, where $\phi \sim 6°$ is the angle between the source trajectory and the fold of the caustic (Gould & Andronov 1999). Then, the apparent caustic-crossing timescale estimated from Δt is $t_{*,\rm app} = (\sin\phi/1.7)\Delta t \sim 0.15$ days, which is about two times shorter than the value estimated from $t_* = \rho t_{\rm E} \sim 0.3$ days. We find that the difference between $t_{*,\rm app}$ and t_* is due to the movement of the caustic caused by the lens-orbital motion. This is shown in Figure 8 where we present the zoom of the caustic configuration around the time of the caustic crossing. It shows that the caustic moves rapidly toward right direction, while the source moves slightly toward left direction. This causes $t_{*,\rm app}$ to be shorter than t_*.

4. Nature of the Lens

4.1. Angular Einstein Radius

From the relations in Equations (2) and (3), one needs two quantities of $\pi_{\rm E}$ and $\theta_{\rm E}$ to uniquely determine the physical parameters of the lens mass and distance. The microlens parallax is estimated from the measured microlens-parallax parameters by $\pi_{\rm E} = (\pi_{{\rm E},N}^2 + \pi_{{\rm E},E}^2)^{1/2}$. The angular Einstein radius is estimated from the measured normalized source radius by $\theta_{\rm E} = \theta_*/\rho$, where the θ_* is the angular source radius. To determine the angular Einstein radius, then we are required to estimate θ_*.

The angular source radius is estimated based on the dereddened color and brightness. To calibrate instrumental color and magnitude, we use the centroid of the red giant clump (RGC), for which the color and brightness are known, as a reference (Yoo et al. 2004). The measured instrumental I-band brightness of the source is $I = 17.19 \pm 0.02$, but the V-band brightness cannot be measured due to the poor photometry caused by severe extinction. Instead of V-band photometry, we use H-band UKIRT data for the color measurement. Figure 9 shows the UKIRT data superposed
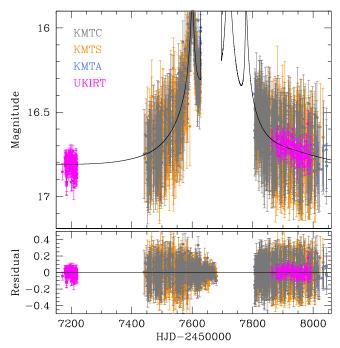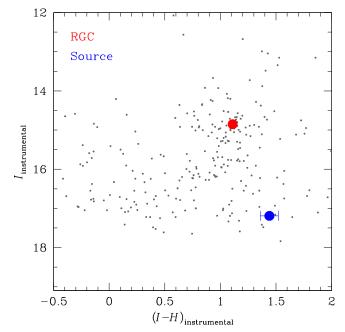

Figure 9. UKIRT data superposed by the model light curve.

Figure 10. Source location with respect to the centroid of RGC in the instrumental $(I - H, I)$ color–magnitude diagram.

by the model curve. From model fitting, we found that the H-band source brightness is $H = 15.75 \pm 0.08$ and thus $I - H = 1.44 \pm 0.08$. To find the reference position of the RGC centroid, we construct an $(I - H, I)$ color–magnitude diagram by matching KMTC I-band and UKIRT H-band data. Figure 10 shows the constructed $(I - H, I)$ color–magnitude diagram. The position of the RGC centroid is $(I - H, I)_{\rm RGC} = (1.11, 14.85)$. From the known values of $(V - I, I)_{\rm 0,RGC} = (1.06, 14, 43)$ (Bensby et al. 2011; Nataf et al. 2013) and using the color–color relation (Bessell & Brett 1988), the dereddened $I - H$ color and I-band magnitude of the RGC centroid are $(I - H, I)_{\rm 0,RGC} = (1.29,$

Table 3
Einstein Radius and Relative Proper Motion

Parameter	$u_0 > 0$	$u_0 < 0$
$\theta_{\rm E}$ (mas)	1.20 ± 0.13	1.14 ± 0.12
$\mu_{\rm geo}$ (mas yr^{-1})	3.91 ± 0.42	3.71 ± 0.40
$\mu_{\rm hel}$ (mas yr^{-1})	2.82 ± 0.30	2.85 ± 0.31
ψ	$21°$	$166°$

Table 4
Physical Lens Parameters

Parameter	$u_0 > 0$	$u_0 < 0$
M_1 ($M_\odot$)	0.34 ± 0.04	0.32 ± 0.04
M_2 ($M_\odot$)	0.17 ± 0.02	0.17 ± 0.02
$D_{\rm L}$ (kpc)	2.14 ± 0.20	2.23 ± 0.20
$a_\perp$ (au)	2.45 ± 0.23	2.43 ± 0.22
$({\rm KE/PE})_\perp$	0.45	0.43

14.43). Combined with the measured offsets in color $\Delta(I - H)$ and magnitude ΔI of the source with respect to the RGC centroid, we find that the dereddened color and brightness of the source are $(I - H, I)_0 = (I - H, I)_{0,\rm RGC} + \Delta(I - H, I) = (1.62 \pm 0.08, 16.77 \pm 0.02)$. The measured $(I - H)_0$ color of the source corresponds to $(V - I)_0 = 1.51$. This, combined with the brightness, indicates that the source is a K-type subgiant. Once the dereddened color of the source is determined, we then convert $V - I$ into $V - K$ using the color–color relation of Bessell & Brett (1988) and then estimate θ_* using the relation between $V - K$ and the surface brightness (Kervella et al. 2004). From this procedure, we find that the angular source radius is $\theta_* = 3.25 \pm 0.34\ \mu$as.

In Table 3, we present the estimated angular Einstein radii for the $u_0 > 0$ and $u_0 < 0$ solutions. Also presented are the relative lens-source proper motions in the geocentric, $\mu_{\rm geo}$, and heliocentric frames, $\mu_{\rm hel}$. They are determined by

$$\boldsymbol{\mu}_{\rm geo} = \frac{\theta_{\rm E}}{t_{\rm E}} \frac{\boldsymbol{\pi}_{\rm E}}{\pi_{\rm E}} \tag{4}$$

and

$$\boldsymbol{\mu}_{\rm hel} = \boldsymbol{\mu}_{\rm geo} + \boldsymbol{v}_{\oplus,\perp} \frac{\pi_{\rm rel}}{\rm au}, \tag{5}$$

respectively (Gould 2004; Dong et al. 2009). Here $\boldsymbol{v}_{\oplus,\perp} = (0.3, 26.0)$ km s^{-1} represents the velocity of the Earth's motion projected on the sky at t_0. The presented angle ψ denotes the orientation angle of $\boldsymbol{\mu}_{\rm hel}$ as measured from the north. We note that the measured value of the relative lens-source proper motion, $\mu_{\rm geo} \sim 3.9$ mas yr^{-1}, is smaller than ~ 5 mas yr^{-1} of typical lensing events. Particularly, the heliocentric proper motion, $\mu_{\rm hel} \sim 2.8$ mas yr^{-1}, is nearly half of the typical value. We will discuss the cause of the slow relative lens-source motion in Section 5.

4.2. Physical Parameters

With the measured angular Einstein radius and the microlens parallax, we determine the mass and distance to the lens using the relations in Equations (2) and (3). In Table 4, we list the masses of the primary, M_1, and companion, M_2, of the lens, distance $D_{\rm L}$, and the projected separation between the lens components, $a_\perp = s D_{\rm L} \theta_{\rm E}$. Also presented is the projected kinetic-to-potential energy ratio that is determined based on the total lens mass $M = M_1 + M_2$, the projected separation $a_\perp$, and the lens-orbital parameters ds/dt and $d\alpha/dt$ by

$$\left(\frac{\rm KE}{\rm PE}\right)_\perp = \frac{(a_\perp/{\rm au})^3}{8\pi^2 (M/M_\odot)} \left[\left(\frac{1}{s}\frac{ds/dt}{\rm yr^{-1}}\right)^2 + \left(\frac{d\alpha/dt}{\rm yr^{-1}}\right)^2\right]. \tag{6}$$

The lens system should meet the requirement $({\rm KE/PE})_\perp \leqslant {\rm KE/PE} \leqslant 1.0$ because otherwise the lens system would not be gravitationally bound. We found that the ratios are

$({\rm KE/PE})_\perp \sim 0.45$ for both $u_0 > 0$ and $u_0 < 0$ solutions, and the solutions meet the requirement. This value is also in the expected range $0.2 \lesssim ({\rm KE/PE})_\perp \lesssim 0.5$ for moderate eccentricity binaries that are not observed at unusual viewing angles.

The estimated masses of the lens components, $M_1 \sim 0.34\ M_\odot$ for the primary and $M_2 \sim 0.17\ M_\odot$ for the companion, correspond to those of a mid- and a late-M-type main-sequence star, respectively. Using the relation in Equation (3), the estimated distance to the lens is $D_{\rm L} \sim 2.1$ kpc. For the determination of $D_{\rm L}$, we use $\pi_{\rm S} = {\rm au}/D_{\rm S}$ with the distance to the source estimated using the relation $D_{\rm S} = d_{\rm GC}/(\cos l + \sin l \cos \theta_{\rm bar}/\sin \theta_{\rm bar}) \sim 8.06$ kpc, where $d_{\rm GC} = 8160$ pc is the Galactocentric distance, $\theta_{\rm bar} = 40°$ is the bulge bar orientation angle, and $l = 0°.58$ is the Galactic longitude of the source (Nataf et al. 2013). The angular Einstein radius is related to the distance to the lens by $\theta_{\rm E} \propto (D_{\rm L}^{-1} - D_{\rm S}^{-1})^{1/2}$, and thus the close distance to the lens results in the large angular Einstein radius. Because $t_{\rm E} = \theta_{\rm E}/\mu$, the long timescale of the event is caused by the combination of the slow relative lens-source motion, and the large Einstein radius due to the close lens distance rather than the heavy mass of the lens.

5. Discussion

Because the event timescale is related to the lens mass and relative lens-source proper motion by $t_{\rm E} \propto \sqrt{M}/\mu$, the long timescale of an event can be ascribed to either a large lens mass or a slow lens-source proper motion. For KMT-2016-BLG-2052, it turns out that the long timescale of the event is caused by the combination of the slow relative lens-source proper motion and the close distance to the lens rather than the heavy mass of the lens. Then, a question is whether KMT-2016-BLG-2052 is an unusual case. A related question is what the probability is for long timescale events to be produced by very heavy lenses such as NSs and BHs. In order answer these questions, we construct the probability distributions of relative lens-source proper motions and lens masses for long timescale events by conducting Monte Carlo simulation of Galactic microlensing events.

The simulation is conducted based on the prior models of the matter density and dynamic distributions and the mass function of lens objects. We adopt the Han & Gould (2003) model for the matter density distribution. In this model, the disk and bulge follow a double-exponential distribution and a triaxial distribution, respectively. The velocity distribution is based on Han & Gould (1995) model. In the model, disk objects move following a Gaussian distribution with a mean corresponding to the disk rotation speed. The motion of bulge objects follows a triaxial Gaussian distribution with the velocity components along the axes determined based on the bulge shape using tensor virial theorem. We use the initial mass function of Chabrier (2003a) for the mass function of Galactic bulge
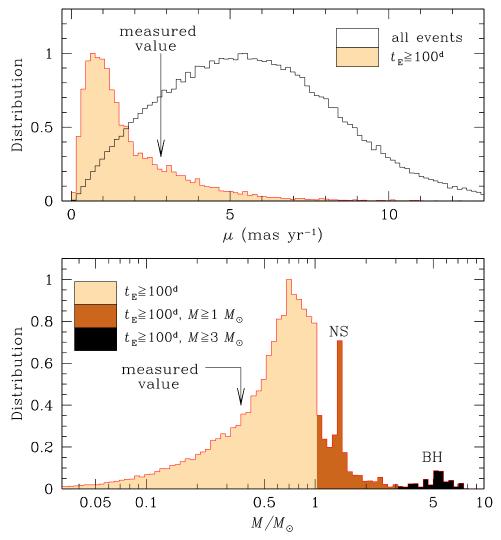
Figure 11. Distributions of the relative lens-source proper motion μ (top panel) and lens mass M (bottom panel) for events with timescale $t_{\rm E} \geqslant 100$ days. For proper motions, we present two distributions where the shaded and unshaded distributions are for events $t_{\rm E} \geqslant 100$ days and for all events regardless of event timescales, respectively. For the lens mass distribution, the regions shaded by dark brown and black colors represent the distributions with lens masses $\geqslant 1.0\, M_\odot$ and $\geqslant 3.0\, M_\odot$, respectively. The values of μ and M indicated by arrows represent the measured values of KMT-2016-BLG-2052L. In the mass distribution, the peaks at $M \sim 1.35\, M_\odot$ and $\sim 5\, M_\odot$ are produced by NSs and BHs, respectively.

objects and the present-day mass function of Chabrier (2003b) for disk objects. We note that the adopted mass functions extend to substellar objects down to $0.01\, M_\odot$. Because stellar remnants can cause long timescale events, we include them in the mass function by assuming that stars with masses $1\, M_\odot \leqslant M < 8\, M_\odot$, $8\, M_\odot \leqslant M < 40\, M_\odot$, and $M \geqslant 40\, M_\odot$ have evolved into white dwarfs (with a mean mass $\langle M \rangle \sim 0.6\, M_\odot$), NSs (with $\langle M \rangle \sim 1.35\, M_\odot$), and BHs (with $\langle M \rangle \sim 5\, M_\odot$), respectively (Gould 2000a).

In Figure 11, we present the distributions of the relative lens-source proper motions (top panel) and lens masses (bottom panel) for events with timescale $t_{\rm E} \geqslant 100$ days. To compare proper motions of long timescale events with those of general events, we also present the proper-motion distribution for all events regardless of event timescales. From the comparison of the proper-motion distributions, one finds that long timescale events tend to have substantially smaller proper motions, with a mode value of ~ 0.8 mas yr^{-1}, than general events, with a mode ~ 5 mas yr^{-1}. The slow relative lens-source proper

motion of long timescale events is most likely caused by the chance alignment of the lens and source motion. Considering that the measured lens-source proper motion of KMT-2016-BLG-2052, $\mu_{\rm hel} \sim 2.8$ mas yr^{-1}, is well within 2σ range of the distribution, the event is not an unusual case of long timescale event. From the distribution of lens masses, we found that the probabilities that long timescale events are produced by lenses with masses $\geqslant 1.0\, M_\odot$ and $\geqslant 3.0\, M_\odot$ are $\sim 19\%$ and 2.6%, respectively. This indicates that the majority of long timescale events are produced by stellar lenses with masses $\lesssim 1.0\, M_\odot$. Considering that events produced by heavy lenses comprise a minor fraction of long timescale events, it is essential to determine the lens mass by measuring both $\pi_{\rm E}$ and $\theta_{\rm E}$ for the firm identification of stellar remnants, such as NSs and BHs.

6. Conclusion

We analyzed the very long timescale binary-lensing event KMT-2016-BLG-2052. We revealed the nature of the lens by

determining the lens mass from the simultaneous measurements of the microlens parallax and the angular Einstein radius. The measured mass indicated that the lens was a binary composed of M dwarfs. We found that the long timescale of the event was caused by the combination of the slow relative lens-source motion and the large angular Einstein radius due to the close distance to the lens rather than the heavy mass of the lens. From the simulation of Galactic lensing events with very long timescales ($t_E \gtrsim 100$ days), we found that long timescale events tend to have substantially slower relative lens-source motions than general events. We also found that the probabilities that long timescale events were produced by lenses with masses $\geqslant 1.0\ M_\odot$ and $\geqslant 3.0\ M_\odot$ are $\sim$19% and 2.6%, respectively, indicating that events produced by heavy lenses comprise a minor fraction of long timescale events. The results indicate that it is essential to determine the lens masses by measuring both π_E and θ_E in order to firmly identify stellar remnants, such as NSs and BHs.

ORCID iDs

Cheongho Han ⓘ https://orcid.org/0000-0002-2641-9964
Woong-Tae Kim ⓘ https://orcid.org/0000-0003-4625-229X
Yoon-Hyun Ryu ⓘ https://orcid.org/0000-0001-9823-2907
In-Gu Shin ⓘ https://orcid.org/0000-0002-4355-9838
Chun-Hwey Kim ⓘ https://orcid.org/0000-0001-8591-4562
Richard W. Pogge ⓘ https://orcid.org/0000-0003-1435-3053
Savannah R. Jacklin ⓘ https://orcid.org/0000-0001-9504-8258

References

Alard, C., & Lupton, R. H. 1998, ApJ, 503, 325
Albrow, M. D., Horne, K., Bramich, D. M., et al. 2009, MNRAS, 397, 2099
Alcock, C., Akerlof, C. W., Allsman, R. A., et al. 1993, Natur, 365, 621
An, J. H., & Gould, A. 2001, ApJL, 563, L111
Aubourg, E., Bareyre, P., Bréhin, S., et al. 1993, Natur, 365, 623
Batista, V., Gould, A., Dieters, S., et al. 2011, A&A, 529, 102
Bensby, T., Adén, D., Meléndez, J., et al. 2011, A&A, 533, A134
Bessell, M. S., & Brett, J. M. 1988, PASP, 100, 1134
Bond, I. A., Abe, F., Dodd, R. J., et al. 2001, MNRAS, 327, 868
Chabrier, G. 2003a, PASP, 115, 763
Chabrier, G. 2003b, ApJL, 586, L133
Dong, S., Gould, A., Udalski, A., et al. 2009, ApJ, 695, 970
Gould, A. 1992, ApJ, 392, 442
Gould, A. 2000a, ApJ, 535, 928
Gould, A. 2000b, ApJ, 542, 785
Gould, A. 2004, ApJ, 606, 319
Gould, A., & Andronov, N. 1999, ApJ, 516, 236
Gould, A., & Loeb, A. 1992, ApJ, 396, 104
Han, C., & Gould, A. 1995, ApJ, 447, 53
Han, C., & Gould, A. 2003, ApJ, 592, 172
Han, C., Udalski, A., Lee, C.-U., et al. 2016, ApJ, 827, 11
Kervella, P., Thévenin, F., Di Folco, E., & Ségransan, D. 2004, A&A, 426, 297
Kim, D.-J., Kim, H.-W., Hwang, K.-H., et al. 2018a, AJ, 155, 76
Kim, H.-W., Hwang, K.-H., Kim, D.-J., et al. 2018b, AJ, 155, 186
Kim, S.-L., Lee, C.-U., Park, B.-G., et al. 2016, JKAS, 49, 37
Mao, S., & Paczynski, B. 1991, ApJL, 374, L37
Nataf, D. M., Gould, A., Fouqué, P., et al. 2013, ApJ, 769, 88
Paczyński, B. 1986, ApJ, 304, 1
Schechter, P. L., Mateo, M., & Saha, A. 1993, PASP, 105, 1342
Shvartzvald, Y., Bryden, G., Gould, A., et al. 2017, AJ, 153, 61
Shvartzvald, Y., Udalski, A., Gould, A., et al. 2015, ApJ, 814, 111
Skowron, J., Udalski, A., Gould, A., et al. 2011, ApJ, 738, 87
Smith, M. C., Mao, S., & Paczyński, B. 2003, MNRAS, 339, 925
Udalski, A., Han, C., & Bozza, V. 2018, ApJ, 853, 70
Udalski, A., Szymański, M., Kałużny, J., et al. 1993, AcA, 43, 289
Udalski, A., Szymański, M. K., & Szymański, G. 2015, AcA, 65, 1
Woźniak, P. R. 2000, AcA, 50, 421
Wyrzykowski, Ł., Kostrzewa-Rutkowska, Z., Skowron, J., et al. 2016, MNRAS, 458, 3012
Yoo, J., DePoy, D. L., Gal-Yam, A., et al. 2004, ApJ, 603, 139